

This work was written as part of one of the author's official duties as an Employee of the United States Government and is therefore a work of the United States Government. In accordance with 17 U.S.C. 105, no copyright protection is available for such works under U.S. Law.

Public Domain Mark 1.0

<https://creativecommons.org/publicdomain/mark/1.0/>

Access to this work was provided by the University of Maryland, Baltimore County (UMBC) ScholarWorks@UMBC digital repository on the Maryland Shared Open Access (MD-SOAR) platform.

Please provide feedback

Please support the ScholarWorks@UMBC repository by emailing scholarworks-group@umbc.edu and telling us what having access to this work means to you and why it's important to you. Thank you.

Solar abundance ratios of the iron-peak elements in the Perseus cluster

Hitomi Collaboration*

The metal abundance of the hot plasma that permeates galaxy clusters represents the accumulation of heavy elements produced by billions of supernovae¹. Therefore, X-ray spectroscopy of the intracluster medium provides an opportunity to investigate the nature of supernova explosions integrated over cosmic time. In particular, the abundance of the iron-peak elements (chromium, manganese, iron and nickel) is key to understanding how the progenitors of typical type Ia supernovae evolve and explode^{2–6}. Recent X-ray studies of the intracluster medium found that the abundance ratios of these elements differ substantially from those seen in the Sun^{7–11}, suggesting differences between the nature of type Ia supernovae in the clusters and in the Milky Way. However, because the K-shell transition lines of chromium and manganese are weak and those of iron and nickel are very close in photon energy, high-resolution spectroscopy is required for an accurate determination of the abundances of these elements. Here we report observations of the Perseus cluster, with statistically significant detections of the resonance emission from chromium, manganese and nickel. Our measurements, combined with the latest atomic models, reveal that these elements have near-solar abundance ratios with respect to iron, in contrast to previous claims. Comparison between our results and modern nucleosynthesis calculations^{12–14} disfavours the hypothesis that type Ia supernova progenitors are exclusively white dwarfs with masses well below the Chandrasekhar limit (about 1.4 times the mass of the Sun). The observed abundance pattern of the iron-peak elements can be explained by taking into account a combination of near- and sub-Chandrasekhar-mass type Ia supernova systems, adding to the mounting evidence that both progenitor types make a substantial contribution to cosmic chemical enrichment^{5,15,16}.

The Soft X-ray Spectrometer (SXS) on board the Hitomi observatory has achieved unprecedented spectral resolution in orbit ($\Delta E \approx 5$ eV in the 2–10 keV band)¹⁷. Figure 1 shows the SXS spectrum of the core of the Perseus cluster (radius r smaller than about $2'$, approximately 40 kpc) in the 1.8–9.0 keV band. This was obtained from the same series of observations as that used in our previous work, which constrained turbulent velocities in the intracluster medium (ICM)¹⁷, but with 25% longer exposure times, which totalled 290 ks. The refined calibration of the effective area of the telescope and the aperture window transmission of the SXS allow the flux measurement of each individual line in the 1.8–9.0 keV band, which encompasses the H- and He-like transitions from Si to Ni.

The excellent performance of the SXS also makes possible the detection of weak He-like resonance lines from Cr, Mn and Ni, with statistical significance of 6σ , 4σ and 12σ , respectively (Fig. 1b, c). Flux measurements of these lines in celestial sources have been extremely challenging with traditional non-dispersive X-ray detectors (such as charge-coupled devices, or CCDs) because such weak features blend into the bremsstrahlung continuum under lower spectral resolution and the Ni xxvii He α and Fe xxv He β lines cannot be resolved (see Fig. 1c).

The hot ICM, confined in the deep gravitational potential well of the cluster, contains the largest fraction (about 80%) of metals in the cluster¹. Among these, the Fe-peak elements (Cr, Mn, Fe and Ni) are

thought to be created predominantly by type Ia supernovae over a cosmological time period^{18,19}. Therefore, the abundance of these elements provides crucial information about the integrated nucleosynthesis in type Ia supernova and its physics.

Despite the importance of type Ia supernovae as distance indicators in cosmology^{20,21}, many of their basic features remain elusive. One important open question is whether the mass of an exploding white dwarf is close to the Chandrasekhar limit ($M_{\text{Ch}} \approx 1.4M_{\odot}$, where M_{\odot} is the mass of the Sun), regardless of whether it originates from a single white dwarf accreting mass from a non-degenerate companion²² or a violent merger of two white dwarfs²³. Recent hydrodynamical simulations show that both delayed-detonation explosions of near- M_{Ch} white dwarfs^{4,12} and full detonations of sub- M_{Ch} white dwarfs^{13,14,24} can reproduce the observed properties (such as optical light curves and spectra) of type Ia supernovae. Therefore, it is difficult to distinguish the two scenarios from optical observations of individual explosions alone.

From the point of view of type Ia supernova nucleosynthesis, the main difference between near- M_{Ch} and sub- M_{Ch} explosions is whether the core of the white dwarf is dense enough for electron capture ($p + e^- \rightarrow n + \nu_e$) to take place during the initial phase of the explosion. The threshold density for this reaction ($\rho_c \approx 10^8 \text{ g cm}^{-3}$) is achieved only when the white dwarf mass is close to M_{Ch} . A distinguishing characteristic of the two models is therefore the production efficiency of neutron-rich species, such as Ni and Mn, which is higher in the near- M_{Ch} scenario^{4–6}. We can use this distinction to identify the dominant system of type Ia supernova progenitor in galaxy clusters by measuring the abundance of the Fe-peak elements in the ICM. The results may apply globally because the large scale of rich galaxy clusters makes them representative of the Universe as a whole.

Here we model the SXS spectrum of the Perseus cluster in the 1.8–9.0 keV band (Fig. 1a) with an optically thin thermal plasma in collisional ionization equilibrium using the latest atomic databases (AtomDB v.3.0.8 and SPEX v.3.03). The emission from the active galactic nucleus (AGN) of the cD galaxy NGC 1275 is taken into account by adding a power law and redshifted Fe I K α_1 and K α_2 lines. Details about the analysis and systematic uncertainty assessment are provided in Methods. Our constraints on the elemental abundances with respect to Fe are shown in Fig. 2 (red circles). These are fully consistent with the latest measured solar abundance ratios²⁵.

Figure 2 also displays previously measured ICM abundances of the core of the Perseus cluster as well as the average abundance of 44 objects, including galaxy clusters, groups and elliptical galaxies, from XMM-Newton (X-ray Multi Mirror Mission) observations (blue triangles and squares)¹¹. This plot highlights some important differences between the measurements. First, the SXS-measured abundances have statistical uncertainties comparable to those of the XMM-Newton results from the combined data of the 44 objects, despite a 15-times-shorter exposure time and a much smaller field of view. Second, while the abundances of Si, S, Ar and Ca obtained in the two studies are consistent, the earlier measurements systematically obtained supersolar abundances of the Fe-peak elements from both the Perseus cluster and the 44-object average.

*A list of participants and their affiliations appears in the online version of the paper.

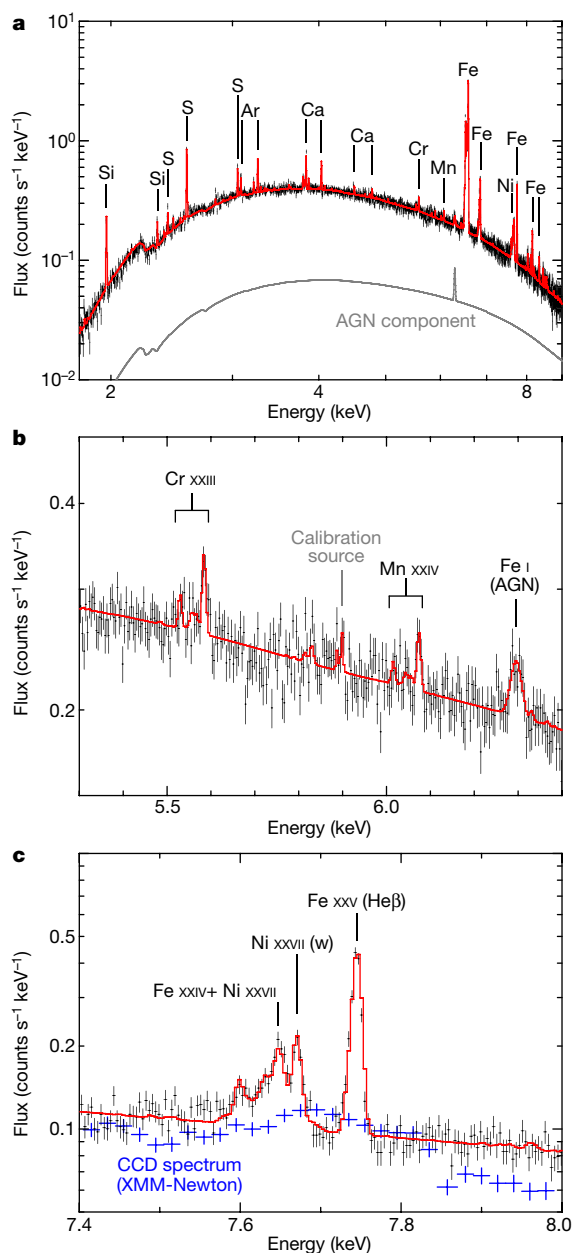


Figure 1 | The Hitomi SXS spectra of the Perseus cluster. **a**, Measured (black) and modelled (red) spectra in the 1.8–9.0 keV band. The modelled spectrum was obtained using an optically thin thermal plasma and the atomic database AtomDB. The error bars represent a 1σ confidence level. The emission from NGC 1275 (AGN) is indicated by the grey curve. The spectrum is rebinned into 4-eV bins for clarity, although 1-eV bins were used for fitting. **b**, Magnified spectrum in the 5.3–6.4 keV band, where the He-like emission from Cr and Mn are detected. The redshifted Fe I fluorescence from the AGN is resolved as well. The label ‘Calibration source’ indicates neutral Mn K α lines, which originate from leakage from the on-board ^{55}Fe calibration source (instrumental origin). **c**, Magnified spectrum in the 7.4–8.0 keV band showing the Ni xxvii resonance (w) line clearly separated from the stronger Fe xxv He β line and other emissions, allowing an accurate measurement of the Ni abundance in a galaxy cluster. For comparison, an XMM-Newton CCD spectrum extracted from the same spatial region is shown (blue data points).

Previous X-ray studies of clusters and elliptical galaxies often obtained a supersolar Ni/Fe abundance ratio, leading to a debate about differences in the nature of type Ia supernovae in early-type galaxies and the Milky Way^{3,7–10}. By contrast, optical spectra of old stars in early-type galaxies indicate that the relative abundances of the Fe-peak elements are consistent with the solar values (see yellow stars in

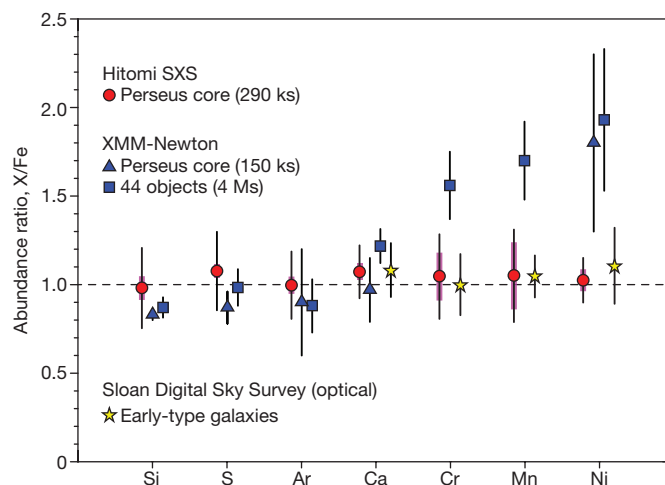


Figure 2 | Elemental abundances of the Perseus cluster. Relative abundances with respect to Fe (X/Fe , $X = \text{Si, S, Ar, Ca, Cr, Mn, Ni}$) normalized to the corresponding solar abundances²⁵ (dashed line). The red circles represent the SXS measurements, with error bars of typical statistical uncertainty at a 1σ confidence level (thick magenta) and systematic uncertainty due to the model selection (thin black; see Methods section ‘Spectral analysis’ for details). The blue triangles and squares represent the XMM-Newton results¹¹ from the core of the Perseus cluster and the integrated data of 44 objects, respectively, with the error bars including both statistical and systematic uncertainties at a 1σ confidence level. The yellow stars show optical measurements of stellar abundances in early-type galaxies from the Sloan Digital Sky Survey²⁶; the error bars include the velocity-dispersion dependence and systematic errors of 0.05 dex. Si is not shown because its abundance is highly sensitive to the velocity dispersion. S and Ar abundances are unavailable in the optical study.

Fig. 2)²⁶. Our X-ray measurement resolves this discrepancy and strongly suggests that the average nature of type Ia supernovae is independent of the star-formation history of their host galaxies. This robust result, which is unaffected by complicated radiative-transfer processes that may lend uncertainty to optical studies, is obtained by accurately determining the Ni abundance using the intensity of its resonance emission line, which is easily resolved from the Fe He β line and other weak emissions of Fe xxiv and Fe xxv in the SXS spectrum.

Because Cr and Mn abundances of individual objects were not constrained by the previous XMM-Newton observations¹¹, we cannot exclude the possibility that sample variance leads, at least in part, to the discrepancy between our results and those of ref. 11. Nevertheless, we demonstrate in Methods that high-resolution spectroscopy is essential for robust measurements of these abundances. In short, only the SXS can clearly separate the weak resonance lines from the continuum component, allowing abundance measurements that are much less subject to systematic uncertainties in spectral modelling. The high-resolution SXS data have also stimulated the development of atomic models, reducing the uncertainties in the modelled line emissivities and improving the accuracy of the abundances with respect to previous work.

Figure 3 compares the SXS-measured abundances of the Fe-peak elements (black data points) with theoretical results from the latest three-dimensional calculations of the near- M_{Ch} type Ia supernova¹² (blue region) and sub- M_{Ch} merger¹³ (green region). We also consider a one-dimensional explosion of a single $1.0M_{\odot}$ white dwarf¹⁴ (grey region) as an alternative example of a sub- M_{Ch} type Ia supernova model. All of these models predict typical type Ia supernova brightness (absolute magnitude -19.3 at the maximum brightness) and a synthesized ^{56}Ni mass of approximately $0.6M_{\odot}$. In addition, they account for contributions of core-collapse supernovae using mass-dependent yields²⁷ averaged over the Salpeter initial mass function (IMF). We allow a conservatively wide range for the fraction of core-collapse supernova, $f_{\text{CC}} \equiv N_{\text{CC}}/(N_{\text{Ia}} + N_{\text{CC}}) = 0.6–0.9$ (typical for cluster cores^{9,19,28,29}), instead of constraining an actual value from our

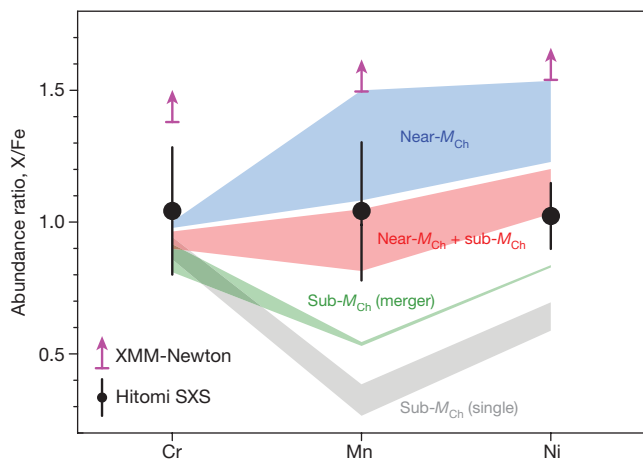


Figure 3 | Comparison between the observed and theoretically calculated abundances of the Fe-peak elements. The black data points are the SXS-measured abundance ratios relative to the solar abundances²⁵ (red circles in Fig. 2). The error bars include both the statistical uncertainty at a 1σ confidence level and the systematic uncertainty. The magenta arrows indicate the 1σ lower limit of the XMM-Newton measurements for the 44 objects¹¹. The blue, green and grey regions represent theoretical predictions for type Ia supernova from the near- M_{Ch} delayed-detonation explosion¹², sub- M_{Ch} violent merger¹³ and single sub- M_{Ch} white dwarf¹⁴ models, respectively, which include contributions from core-collapse supernovae²⁷ (CC). The red region corresponds to a model that assumes equal contributions from near- M_{Ch} type Ia supernovae and sub- M_{Ch} violent mergers, which provides a reasonable fit to the data (although the exact ratio between the two supernova types is subject to uncertainties in the model parameters).

observation (see Methods for more details). As expected, the near- M_{Ch} model predicts higher abundances of Mn and Ni due to the efficient electron capture in exploding white dwarfs. The observed abundance pattern disfavors the hypothesis that all type Ia supernovae involve sub- M_{Ch} white dwarfs and supports the combination of near- M_{Ch} and sub- M_{Ch} type Ia supernovae with roughly equal numbers (red region in the Fig. 3). We also find that our result starkly contrasts previous claims that the introduction of rather non-standard full-deflagration type Ia supernova models is required to explain a Ni/Fe ratio that was estimated to be much higher^{3,7} than our measurement. In Methods, we investigate other type Ia and core-collapse supernova models and find that our main conclusion remains valid, although the exact ratio of near- M_{Ch} to sub- M_{Ch} contributions may depend on the model details.

The Hitomi SXS observation has demonstrated the power of high-resolution X-ray spectroscopy: measurement of the chemical enrichment of a single object has provided new insight into fundamental phenomena that shape the present-day Universe. A common abundance pattern between the solar neighbourhood and the Perseus cluster suggests that the chemical composition of the Sun is probably a good indicator of the nature of the average type Ia supernova in the Universe. To confirm this conclusion, it is extremely important to scrutinize other environments, such as the outskirts of galaxy clusters³⁰, at high spectral resolution in future X-ray observatories.

Online Content Methods, along with any additional Extended Data display items and Source Data, are available in the online version of the paper; references unique to these sections appear only in the online paper.

Received 2 June; accepted 21 September 2017.

Published online 13 November 2017.

1. Mushotzky, R. *et al.* Measurement of the elemental abundances in four rich clusters of galaxies. I. Observations. *Astrophys. J.* **466**, 686–694 (1996).
2. Finoguenov, A., Matsushita, K., Böhringer, H., Ikebe, Y. & Arnaud, M. X-ray evidence for spectroscopic diversity of type Ia supernovae. XMM observation of the elemental abundance pattern in M 87. *Astron. Astrophys.* **381**, 21–31 (2002).
3. Mernier, F. *et al.* Origin of central abundances in the hot intra-cluster medium. II. Chemical enrichment and supernova yield models. *Astron. Astrophys.* **595**, A126 (2016).

4. Maeda, K. *et al.* Nebular spectra and explosion asymmetry of Type Ia supernovae. *Astrophys. J.* **708**, 1703–1715 (2010).
5. Seitzzahl, I. R., Cescutti, G., Röpke, F. K., Ruiter, A. J. & Pakmor, R. Solar abundance of manganese: a case for near Chandrasekhar-mass Type Ia supernova progenitors. *Astron. Astrophys.* **559**, L5 (2013).
6. Yamaguchi, H. *et al.* A Chandrasekhar mass progenitor for the Type Ia supernova remnant 3C 397 from the enhanced abundances of nickel and manganese. *Astrophys. J.* **801**, L31 (2015).
7. Dupke, R. A. & White, R. E. III. Constraints on type Ia supernova models from X-ray spectra of galaxy clusters. *Astrophys. J.* **528**, 139–144 (2000).
8. Gastaldello, F. & Molendi, S. Ni abundance in the core of the Perseus cluster: an answer to the significance of resonant scattering. *Astrophys. J.* **600**, 670–680 (2004).
9. De Plaa, J. *et al.* Constraining supernova models using the hot gas in clusters of galaxies. *Astron. Astrophys.* **465**, 345–355 (2007).
10. De Grandi, S. & Molendi, S. Metal abundances in the cool cores of galaxy clusters. *Astron. Astrophys.* **508**, 565–574 (2009).
11. Mernier, F. *et al.* Origin of central abundances in the hot intra-cluster medium. I. Individual and average abundance ratios from XMM-Newton EPIC. *Astron. Astrophys.* **592**, A157 (2016).
12. Seitzzahl, I. R. *et al.* Three-dimensional delayed-detonation models with nucleosynthesis for Type Ia supernovae. *Mon. Not. R. Astron. Soc.* **429**, 1156–1172 (2013).
13. Pakmor, R. *et al.* Normal type Ia supernovae from violent mergers of white dwarf binaries. *Astrophys. J.* **747**, L10 (2012).
14. Woosley, S. E. & Kasen, D. Sub-Chandrasekhar mass models for supernovae. *Astrophys. J.* **734**, 38 (2011).
15. Scalzo, R. A., Ruiter, A. J. & Sim, S. A. The ejected mass distribution of Type Ia supernovae: a significant rate of non-Chandrasekhar-mass progenitors. *Mon. Not. R. Astron. Soc.* **445**, 2535–2544 (2014).
16. Blondin, S., Dessart, L., Hillier, D. J. & Khokhlov, A. M. Evidence for sub-Chandrasekhar-mass progenitors of Type Ia supernovae at the faint end of the width-luminosity relation. *Mon. Not. R. Astron. Soc.* **470**, 157–165 (2017).
17. Hitomi Collaboration. The quiescent intracluster medium in the core of the Perseus cluster. *Nature* **535**, 117–121 (2016).
18. Loewenstein, M. & Mushotzky, R. F. Measurement of the elemental abundances in four rich clusters of galaxies. II. The initial mass function and mass loss in elliptical galaxies, enrichment, and energetics in the ICM. *Astrophys. J.* **466**, 695–703 (1996).
19. Matsushita, K., Sakuma, E., Sasaki, T., Sato, K. & Simionescu, A. Metal-mass-to-light ratios of the Perseus cluster out to the virial radius. *Astrophys. J.* **764**, 147 (2013).
20. Riess, A. G. *et al.* Observational evidence from supernovae for an accelerating universe and a cosmological constant. *Astron. J.* **116**, 1009–1038 (1998).
21. Perlmutter, S. *et al.* Measurements of Ω and Λ from 42 high-redshift supernovae. *Astrophys. J.* **517**, 565–586 (1999).
22. Whelan, J. & Iben, I. Jr. Binaries and supernovae of type I. *Astrophys. J.* **186**, 1007–1014 (1973).
23. Webbink, R. F. Double white dwarfs as progenitors of R Coronae Borealis stars and Type I supernovae. *Astrophys. J.* **277**, 355–360 (1984).
24. Sim, S. A. *et al.* Detonations in sub-Chandrasekhar-mass C+O white dwarfs. *Astrophys. J.* **714**, L52–L57 (2010).
25. Lodders, K., Palme, H. & Gail, H.-P. In *Solar System* (ed. Trümper, J. E.) 712–770 (Vol. VI/4B of *Landolt Börnstein, New Series*, Springer, 2009).
26. Conroy, C., Graves, G. J. & van Dokkum, P. G. Early-type galaxy archaeology: ages, abundance ratios, and effective temperatures from full-spectrum fitting. *Astrophys. J.* **780**, 33 (2013).
27. Nomoto, K., Kobayashi, C. & Tominaga, N. Nucleosynthesis in stars and the chemical enrichment of galaxies. *Annu. Rev. Astron. Astrophys.* **51**, 457–509 (2013).
28. Sato, K. *et al.* Type Ia and II supernovae contributions to metal enrichment in the intracluster medium observed with Suzaku. *Astrophys. J.* **667**, L41–L44 (2007).
29. Bulbul, E., Smith, R. K. & Loewenstein, M. A new method to constrain supernova fractions using X-ray observations of clusters of galaxies. *Astrophys. J.* **753**, 54 (2012).
30. Werner, N., Urban, O., Simionescu, A. & Allen, S. W. A uniform metal distribution in the intergalactic medium of the Perseus cluster of galaxies. *Nature* **502**, 656–658 (2013).

Supplementary Information is available in the online version of the paper.

Acknowledgements Acknowledgements are provided in the Supplementary Information.

Author Contributions H.Y. wrote the manuscript. H.Y., S.N., A. Simionescu, E.B. and M.L. analysed the data. H.Y., K. Matsushita, M.L., A. Simionescu, S.N., K.S. and R.M. discussed the results. Y. Ishisaki confirmed the reliability of the observed results using his expertise in the SXS signal processing system. The science goals of Hitomi were discussed and developed over more than 10 years by the ASTRO-H Science Working Group (SWG), all members of which are authors of this manuscript. All the instruments were prepared by the joint efforts of the team. Calibration of the Perseus dataset was carried out by members of the SXS team. The manuscript was subject to an internal collaboration-wide review process. All authors reviewed and approved the final version of the manuscript.

Author Information Reprints and permissions information is available at www.nature.com/reprints. The authors declare no competing financial interests. Readers are welcome to comment on the online version of the paper. Publisher's note: Springer Nature remains neutral with regard to jurisdictional claims in published maps and institutional affiliations. Correspondence and requests for materials should be addressed to H.Y. (hiroya.yamaguchi@nasa.gov) and K. Matsushita (matsushita@rs.kagu.tus.ac.jp).

Hitomi Collaboration

Felix Aharonian^{1,2,3}, Hiroki Akamatsu⁴, Fumie Akimoto⁵, Steven W. Allen^{6,7,8}, Lorella Angelini⁹, Marc Audard¹⁰, Hisamitsu Awaki¹¹, Magnus Axelsson¹², Aya Bamba^{13,14}, Marshall W. Bautz¹⁵, Roger Blandford^{6,7,8}, Laura W. Brenneman¹⁶, Gregory V. Brown¹⁷, Esra Bulbul^{15,16}, Edward M. Cackett¹⁸, Maria Chernyakova¹, Meng P. Chiao⁹, Paolo S. Coppi^{19,20}, Elisa Costantini⁴, Jelle de Plaa⁴, Jan-Willem den Herder⁴, Chris Done²¹, Tadayasu Dotani²², Ken Ebisawa²², Megan E. Eckart⁹, Teruaki Enoto^{23,24}, Yuichiro Ezoe²⁵, Andrew C. Fabian²⁶, Carlo Ferrigno¹⁰, Adam R. Foster¹⁶, Ryuichi Fujimoto²⁷, Yasushi Fukazawa²⁸, Akihiro Furuzawa²⁹, Massimiliano Galeazzi³⁰, Luigi C. Gallo³¹, Poshak Gandhi³², Margherita Giustini⁴, Andrea Goldwurm^{33,34}, Liyi Gu⁴, Matteo Guainazzi³⁵, Yoshito Haba³⁶, Kouichi Hagino³⁷, Kenji Hamaguchi^{9,38}, Ilana M. Harrus^{9,38}, Isamu Hatsukade³⁹, Katsuhiro Hayashi^{22,40}, Takayuki Hayashi⁴⁰, Kiyoishi Hayashida⁴¹, Junko S. Hiraga⁴², Ann Hornschemeier⁹, Akio Hoshino⁴³, John P. Hughes⁴⁴, Yuto Ichinohe²⁵, Ryo Iizuka²², Hajime Inoue⁴⁵, Yoshiyuki Inoue²², Manabu Ishida²², Kumi Ishikawa²², Yoshitaka Ishisaki²⁵, Masachika Iwai²², Jelle Kaastra^{4,46}, Tim Kallman⁹, Tsuneyoshi Kamae¹³, Jun Kataoka⁴⁷, Satoru Katsuda⁴⁸, Nobuyuki Kawai⁴⁹, Richard L. Kelley⁹, Caroline A. Kilbourne⁹, Takao Kitaguchi²⁸, Shunji Kitamoto⁴³, Tetsu Kitayama⁵⁰, Takayoshi Kohmura³⁷, Motohide Kokubun²², Katsuji Koyama⁵¹, Shu Koyama²², Peter Kretschmar⁵², Hans A. Krimm^{53,54}, Aya Kubota⁵⁵, Hideyo Kunieda⁴⁰, Philippe Laurent^{33,34}, Shiu-Hang Lee²³, Maurice A. Leutenegger^{9,38}, Olivier Limousine³⁴, Michael Loewenstein^{9,56}, Knox S. Long³⁷, David Lumb³⁵, Greg Madejski⁶, Yoshitomo Maeda²², Daniel Maier^{33,34}, Kazuo Makishima⁵⁸, Maxim Markevitch⁹, Hironori Matsumoto⁴¹, Kyoko Matsushita⁵⁹, Dan McCammon⁶⁰, Brian R. McNamara⁶¹, Missagh Mehdipour⁴, Eric D. Miller¹⁵, Jon M. Miller⁶², Shin Mineshige²², Kazuhisa Mitsuda²², Ikuyuki Mitsuishi⁴⁰, Takuya Miyazawa⁶³, Tsunefumi Mizuno^{28,64}, Hideyuki Mori⁹, Koji Mori³⁹, Koji Mukai^{9,38}, Hiroshi Murakami⁶⁵, Richard F. Mushotzky³⁶, Takao Nakagawa²², Hiroshi Nakajima⁴¹, Takeshi Nakamori⁶⁶, Shinya Nakashima⁵⁸, Kazuhiro Nakazawa^{13,14}, Kumiko K. Nobukawa⁶⁷, Masayoshi Nobukawa⁶⁸, Hirofumi Noda^{69,70}, Hirokazu Odaka⁶, Takaya Ohashi²⁵, Masanori Ohno²⁸, Takashi Okajima⁹, Naomi Ota⁶⁷, Masanobu Ozaki²², Frits Paerels⁷¹, Stéphane Paltani¹⁰, Robert Petre⁹, Ciro Pinto²⁶, Frederick S. Porter⁹, Katja Pottschmidt^{9,38}, Christopher S. Reynolds⁵⁶, Samar Safi-Harb⁷², Shinya Saito⁴³, Kazuhiro Sakai⁹, Toru Sasaki⁵⁹, Goro Sato²², Kosuke Sato⁵⁹, Rie Sato²², Makoto Sawada⁷³, Norbert Schartel⁵², Peter J. Serlemitsos⁹, Hiromi Seta²⁵, Megumi Shidatsu⁵⁸, Aurora Simionescu²², Randall K. Smith¹⁶, Yang Soong⁹, Lukasz Stawarz⁷⁴, Yoyoharu Sugawara²², Satoshi Sugita⁴⁹, Andrew Szymkowiak²⁰, Hiroyasu Tajima⁵, Hiromitsu Takahashi²⁸, Tadayuki Takahashi²², Shin'ichiro Takeda⁶³, Yoh Takei²², Toru Tamagawa⁷⁵, Takayuki Tamura²², Takaaki Tanaka⁵¹, Yasuo Tanaka^{22,76}, Yasuyuki T. Tanaka²⁸, Makoto S. Tashiro⁷⁷, Yuzuru Tawara⁴⁰, Yukikatsu Terada⁷⁷, Yuichi Terashima¹¹, Francesco Tombesi^{9,56,78}, Hiroshi Tomida²², Yohko Tsuboi⁴⁸, Masahiro Tsujimoto²², Hiroshi Tsunemi⁴¹, Takeshi Go Tsuru⁵¹, Hiroyuki Uchida⁵¹, Hideki Uchiyama⁷⁹, Yasunobu Uchiyama⁴³, Shutaro Ueda²², Yoshihiro Ueda²³, Shin'ichiro Uno⁸⁰, C. Megan Urry²⁰, Eugenio Ursino³⁰, Cor P. de Vries⁴, Shin Watanabe²², Norbert Werner^{28,81,82}, Daniel R. Wik^{9,83,84}, Dan R. Wilkins⁶, Brian J. Williams⁵⁷, Shinya Yamada²⁵, Hiroya Yamaguchi^{9,56}, Kazutaka Yamaoka^{5,40}, Noriko Y. Yamasaki²², Makoto Yamauchi³⁹, Shigeo Yamauchi⁶⁷, Tahir Yaqoob^{9,38}, Yoichi Yatsu⁴⁹, Daisuke Yonetoku²⁷, Irina Zhuravleva^{6,7} & Abderahmen Zoghbi⁶²

¹Dublin Institute for Advanced Studies, 31 Fitzwilliam Place, Dublin 2, Ireland. ²Max-Planck-Institut für Kernphysik, PO Box 103980, 69029 Heidelberg, Germany. ³Gran Sasso Science Institute, viale Francesco Crispi 7, 67100 L' Aquila, Italy. ⁴SRON Netherlands Institute for Space Research, Sorbonnelaan 2, 3584 CA Utrecht, The Netherlands. ⁵Institute for Space-Earth Environmental Research, Nagoya University, Furo-cho, Chikusa-ku, Nagoya, Aichi 464-8601, Japan. ⁶Kavli Institute for Particle Astrophysics and Cosmology, Stanford University, 452 Lomita Mall, Stanford, California 94305, USA. ⁷Department of Physics, Stanford University, 382 Via Pueblo Mall, Stanford, California 94305, USA. ⁸SLAC National Accelerator Laboratory, 2575 Sand Hill Road, Menlo Park, California 94025, USA. ⁹NASA, Goddard Space Flight Center, 8800 Greenbelt Road, Greenbelt, Maryland 20771, USA. ¹⁰Department of Astronomy, University of Geneva, ch. d'Écogia 16, CH-1290 Versoix, Switzerland. ¹¹Department of Physics, Ehime University, Bunkyo-cho, Matsuyama, Ehime 790-8577, Japan. ¹²Department of Physics and Oskar Klein Center, Stockholm University, 106 91 Stockholm, Sweden. ¹³Department of Physics, The University of Tokyo, 7-3-1 Hongo, Bunkyo-ku, Tokyo 113-0033, Japan. ¹⁴Research Center for the Early Universe, School of Science, The University of Tokyo, 7-3-1 Hongo, Bunkyo-ku, Tokyo 113-0033, Japan. ¹⁵Kavli Institute for Astrophysics and Space Research, Massachusetts Institute of Technology, 77 Massachusetts Avenue, Cambridge, Massachusetts 02139, USA. ¹⁶Smithsonian Astrophysical Observatory, 60 Garden Street, MS-4 Cambridge, Massachusetts 02138, USA. ¹⁷Lawrence Livermore National Laboratory, 7000 East Avenue, Livermore, California 94550, USA. ¹⁸Department of Physics and Astronomy, Wayne State

University, 666 West Hancock Street, Detroit, Michigan 48201, USA. ¹⁹Astronomy Department, Yale University, New Haven, Connecticut 06520-8101, USA. ²⁰Physics Department, Yale University, New Haven, Connecticut 06520-8120, USA. ²¹Centre for Extragalactic Astronomy, Department of Physics, University of Durham, South Road, Durham DH1 3LE, UK. ²²Japan Aerospace Exploration Agency, Institute of Space and Astronautical Science, 3-1-1 Yoshino-dai, Chuo-ku, Sagami-hara, Kanagawa 252-5210, Japan. ²³Department of Astronomy, Kyoto University, Kitashirakawa-Oiwake-cho, Sakyo-ku, Kyoto 606-8502, Japan. ²⁴The Hakubi Center for Advanced Research, Kyoto University, Kyoto 606-8302, Japan. ²⁵Department of Physics, Tokyo Metropolitan University, 1-1 Minami-Osawa, Hachioji, Tokyo 192-0397, Japan. ²⁶Institute of Astronomy, University of Cambridge, Madingley Road, Cambridge CB3 0HA, UK. ²⁷Faculty of Mathematics and Physics, Kanazawa University, Kakuma-machi, Kanazawa, Ishikawa 920-1192, Japan. ²⁸School of Science, Hiroshima University, 1-3-1 Kagamiyama, Higashi-Hiroshima 739-8526, Japan. ²⁹Fujita Health University, Toyoake, Aichi 470-1192, Japan. ³⁰Physics Department, University of Miami, 1320 Campo Sano Drive, Coral Gables, Florida 33146, USA. ³¹Department of Astronomy and Physics, Saint Mary's University, 923 Robie Street, Halifax, Nova Scotia B3H 3C3, Canada. ³²Department of Physics and Astronomy, University of Southampton, Highfield, Southampton SO17 1BJ, UK. ³³Laboratoire APC, 10 rue Alice Domon et Léonie Duquet, 75013 Paris, France. ³⁴CEA Saclay, 91191 Gif sur Yvette, France. ³⁵European Space Research and Technology Center, Keplerlaan 1, 2201 AZ Noordwijk, The Netherlands. ³⁶Department of Physics and Astronomy, Aichi University of Education, Aichi 448-8543, Japan. ³⁷Department of Physics, Tokyo University of Science, 2641 Yamazaki, Noda, Chiba 278-8510, Japan. ³⁸Department of Physics, University of Maryland Baltimore County, 1000 Hilltop Circle, Baltimore, Maryland 21250, USA. ³⁹Department of Applied Physics and Electronic Engineering, University of Miyazaki, 1-1 Gakuen Kibanadai-Nishi, Miyazaki 889-2192, Japan. ⁴⁰Department of Physics, Nagoya University, Furo-cho, Chikusa-ku, Nagoya, Aichi 464-8602, Japan. ⁴¹Department of Earth and Space Science, Osaka University, 1-1 Machikaneyama-cho, Toyonaka, Osaka 560-0043, Japan. ⁴²Department of Physics, Kwansei Gakuin University, 2-1 Gakuen, Sanda, Hyogo 669-1337, Japan. ⁴³Department of Physics, Rikkyo University, 3-34-1 Nishi-Ikebukuro, Toshima-ku, Tokyo 171-8501, Japan. ⁴⁴Department of Physics and Astronomy, Rutgers University, 136 Frelinghuysen Road, Piscataway, New Jersey 08854, USA. ⁴⁵Meisei University, 2-1-1 Hodokubo, Hino, Tokyo 191-8506, Japan. ⁴⁶Leiden Observatory, Leiden University, PO Box 9513, 2300 RA Leiden, The Netherlands. ⁴⁷Research Institute for Science and Engineering, Waseda University, 3-4-1 Ohkubo, Shinjuku, Tokyo 169-8555, Japan. ⁴⁸Department of Physics, Chuo University, 1-13-27 Kasuga, Bunkyo, Tokyo 112-8551, Japan. ⁴⁹Department of Physics, Tokyo Institute of Technology, 2-12-1 Ookayama, Meguro-ku, Tokyo 152-8550, Japan. ⁵⁰Department of Physics, Toho University, 2-2-1 Miyama, Funabashi, Chiba 274-8510, Japan. ⁵¹Department of Physics, Kyoto University, Kitashirakawa-Oiwake-cho, Sakyo, Kyoto 606-8502, Japan. ⁵²European Space Astronomy Center, Camino Bajo del Castillo s/n, 28692 Villanueva de la Cañada, Madrid, Spain. ⁵³Universities Space Research Association, 7178 Columbia Gateway Drive, Columbia, Maryland 21046, USA. ⁵⁴National Science Foundation, 4201 Wilson Blvd, Arlington, Virginia 22230, USA. ⁵⁵Department of Electronic Information Systems, Shibaura Institute of Technology, 307 Fukasaku, Minuma-ku, Saitama-shi, Saitama 337-8570, Japan. ⁵⁶Department of Astronomy, University of Maryland, College Park, Maryland 20742, USA. ⁵⁷Space Telescope Science Institute, 3700 San Martin Drive, Baltimore, Maryland 21218, USA. ⁵⁸Institute of Physical and Chemical Research, 2-1 Hirosawa, Wako, Saitama 351-0198, Japan. ⁵⁹Department of Physics, Tokyo University of Science, 1-3 Kagurazaka, Shinjuku-ku, Tokyo 162-8601, Japan. ⁶⁰Department of Physics, University of Wisconsin, Madison, Wisconsin 53706, USA. ⁶¹Department of Physics and Astronomy, University of Waterloo, 200 University Avenue West, Waterloo, Ontario N2L 3G1, Canada. ⁶²Department of Astronomy, University of Michigan, 1085 South University Avenue, Ann Arbor, Michigan 48109, USA. ⁶³Okinawa Institute of Science and Technology Graduate University, 1919-1 Tancha, Onna-son Okinawa 904-0495, Japan. ⁶⁴Hiroshima Astrophysical Science Center, Hiroshima University, Higashi-Hiroshima, Hiroshima 739-8526, Japan. ⁶⁵Faculty of Liberal Arts, Tohoku Gakuin University, 2-1-1 Tenjinzawa, Izumi-ku, Sendai, Miyagi 981-3193, Japan. ⁶⁶Faculty of Science, Yamagata University, 1-4-12 Kojirakawa-machi, Yamagata, Yamagata 990-8560, Japan. ⁶⁷Department of Physics, Nara Women's University, Kitaoyanishi-machi, Nara, Nara 630-8506, Japan. ⁶⁸Department of Teacher Training and School Education, Nara University of Education, Takabatake-cho, Nara 630-8528, Japan. ⁶⁹Frontier Research Institute for Interdisciplinary Sciences, Tohoku University, 6-3 Aramaki-zaaoba, Aoba-ku, Sendai, Miyagi 980-8578, Japan. ⁷⁰Astronomical Institute, Tohoku University, 6-3 Aramaki-zaaoba, Aoba-ku, Sendai, Miyagi 980-8578, Japan. ⁷¹Astrophysics Laboratory, Columbia University, 550 West 120th Street, New York, New York 10027, USA. ⁷²Department of Physics and Astronomy, University of Manitoba, Winnipeg, Manitoba R3T 2N2, Canada. ⁷³Department of Physics and Mathematics, Aoyama Gakuin University, 5-10-1 Fuchinobe, Chuo-ku, Sagami-hara, Kanagawa 252-5258, Japan. ⁷⁴Astronomical Observatory of Jagiellonian University, ul. Orla 171, 30-244 Kraków, Poland. ⁷⁵RIKEN Nishina Center, 2-1 Hirosawa, Wako, Saitama 351-0198, Japan. ⁷⁶Max Planck Institute for extraterrestrial Physics, Giessenbachstrasse 1, 85748 Garching, Germany. ⁷⁷Department of Physics, Saitama University, 255 Shimo-Okubo, Sakura-ku, Saitama, 338-8570, Japan. ⁷⁸Department of Physics, University of Rome 'Tor Vergata', Via della Ricerca Scientifica 1, I-00133 Rome, Italy. ⁷⁹Faculty of Education, Shizuoka University, 836 Ohya, Suruga-ku, Shizuoka 422-8529, Japan. ⁸⁰Faculty of Health Sciences, Nihon Fukushi University, 26-2 Higashi Haemi-cho, Handa, Aichi 475-0012, Japan. ⁸¹MTA-Eötvös University Lendület Hot Universe Research Group, Pázmány Péter sétány 1/A, Budapest 1117, Hungary. ⁸²Department of Theoretical Physics and Astrophysics, Faculty of Science, Masaryk University, Kotlářská 2, Brno 611 37, Czech Republic. ⁸³Department of Physics and Astronomy, University of Utah, 115 South 1400 East, Salt Lake City, Utah 84112, USA. ⁸⁴The Johns Hopkins University, Homewood Campus, Baltimore, Maryland 21218, USA.

METHODS

Observations and data reduction. The Hitomi observations of the Perseus cluster core were performed using the SXS in the sequences summarized in Extended Data Table 1. The SXS field of view in each sequence is indicated in Extended Data Fig. 1. The data from the first four sequences, which had almost identical aim points, were also used in our previous work¹⁷. The spacecraft attitude was slightly different for the last sequence, so that the nucleus of NGC 1275 was observed using the central pixels of the SXS. The aperture window, which consists of a 262- μm Be filter and several contaminant materials³¹, was not opened before the loss of the mission. This filter substantially attenuated X-rays incident on the SXS effective area, especially in the soft-X-ray band, limiting the SXS bandpass to above about 1.8 keV.

The data reduction was made with tools from the Hitomi software package, which is publicly available from NASA's HEASARC archive (<https://heasarc.gsfc.nasa.gov/docs/software/lheasoft/download.html>). We used cleaned event data of the latest release version with the standard screening for the post-pipeline processes³². The spectral analysis was performed using only high-resolution primary events, which have the best energy resolution. The redistribution matrix file was generated with the extra-large size option, which accounts for all components of the line spread function, including the main peak, low-energy exponential tail, escape peaks and electron-loss continuum^{31,33}. The full-width at half-maximum of the main-peak component was measured to be 4.9 eV for the ⁵⁵Fe calibration source^{34,35}.

Additional gain correction. Because of the short life of the mission (launched on 17 February 2017, lost on 26 March 2017), opportunities for on-board calibration were limited. This caused some uncertainty in the detector gain (pulse height–energy conversion factors), particularly at energies far from the Mn K α lines (5.9 keV) from the on-board ⁵⁵Fe calibration source. We thus applied the following gain calibration and correction using the Perseus data, in addition to the original calibration, which is described in ref. 17.

First, we modelled the Fe He α complex with an ionization equilibrium plasma for each pixel in each sequence listed in Extended Data Table 1 (sequences 100040030–100040050 were combined together because they were parts of a continuous observation with almost identical instrumental conditions). Then, we scaled the spectrum with a linear function such that the Fe He α energies matched the theoretical values at the redshift of NGC 1275 ($z = 0.01756$)³⁶. We then merged the data of all the pixels and measured the X-ray energies of the detected lines. The differences between the measured and theoretical energies are plotted in Extended Data Fig. 2. The discrepancy, although small, increases towards lower and higher energies with respect to the calibration source line (5.9 keV). We empirically fitted these plots with a parabolic function and then updated the pulse-invariant spectral channel of each detected event using the derived coefficients. We note that this empirical correction method should not be used outside of the range of the fit; in particular, the actual gain error must be almost zero at the energies near 0 eV. The data from all sequences were then combined to increase the photon statistics, and the merged, gain-corrected spectrum was used thereafter. When generating the telescope response to the merged data, we also took into account the off-axis effective area of the Soft X-ray Telescope³⁷, which focuses incoming photons on the SXS pixels at the focal plane.

Spectral analysis. We analysed the SXS spectrum in the 1.8–9.0 keV band with an energy bin size of 1 eV. The spectral fitting was made using the C-statistic³⁸ without subtracting any background components because the background level was negligibly low (about 7×10^{-4} counts $\text{s}^{-1} \text{keV}^{-1}$ for the entire field of view), with even its strongest emission lines well below the source flux in the 1.8–9.0 keV energy band. In fact, we found no significant change in the spectral parameters when we fitted the source spectrum by simultaneously modelling instrumental background data extracted from night-Earth observations. The cosmic X-ray background is also negligible at this cluster core region, well below 1% of the source emission over the entire energy band³⁹.

We fitted the spectrum of the Perseus cluster with a single-temperature optically thin thermal plasma model (bvapec model in the XSPEC package) using the latest version of the atomic database AtomDB v.3.0.8⁴⁰. The fitted parameters included the electron temperature (kT_e), redshift (z), turbulence velocity, emission measure and the elemental abundances of Si, S, Ar, Ca, Cr, Mn, Fe and Ni relative to the solar values (Extended Data Table 2)²⁵. We included a power-law component and the redshifted lines of the Fe $\text{K}\alpha$ fluorescence (6.4 keV in the rest frame) to account for the emission from the AGN of NGC 1275⁴¹. We determined the photon index and flux of the power-law component to be $\Gamma \approx 1.9$ and $F_{2-10 \text{ keV}} \approx 3 \times 10^{-11} \text{ erg s}^{-1} \text{ cm}^{-2}$, respectively, by using an AGN-dominated spectrum derived by SXS image analysis decomposing AGN and ICM emissions, and we applied these values in the analysis of the ICM spectrum (Fig. 1) that was extracted from the entire SXS array. A foreground absorption column was fixed at $1.38 \times 10^{21} \text{ cm}^{-2}$ (ref. 42). The possible effect of resonance scattering^{17,43} was accounted for by adding a Gaussian at the energy of the Fe xxv resonance line with a negative flux.

Weak ⁵⁵Fe calibration source leakage events were taken into account by adding narrow Gaussians at the theoretical energies of the Mn K α lines, although this had no impact on our analysis results. With this model (model A1), we obtained a best-fit value of $kT_e = 3.97 \pm 0.02 \text{ keV}$ and an absolute Fe abundance (that is, the Fe/H number ratio relative to the solar value) 0.63 ± 0.01 , with a C-statistic and χ^2 of 7,483 and 7,862, respectively (7,180 degrees of freedom). The relative abundances of the other elements (with respect to Fe) are shown in Extended Data Fig. 3. The uncertainty in our gain correction is smaller than 1 eV at energies near the Mn K α calibration lines (Extended Data Fig. 3), and thus its effect on the determination of the Fe-peak element abundances is negligible.

We estimated systematic uncertainties in the measured abundances by introducing different models and assumptions. First, we excluded the resonance-scattering correction, that is, the negative-flux Fe xxv line (model A2). This did not change the relative abundances substantially, confirming previous suggestions that the resonance-scattering effect is negligible in abundance measurements^{39,41}. We also fitted the spectrum with two-temperature models, with and without the resonance-scattering effect (models A3 and A4, respectively). In these models, all parameters—except the temperatures and emission measures—of two plasma components with different temperatures were constrained to have identical values. For model A3, we obtained best-fit temperatures of $kT_{e1} = 4.04 \pm 0.05 \text{ keV}$ and $kT_{e2} = 1.60 \pm 0.27 \text{ keV}$, with the 2–10-keV flux of the higher-temperature component being 30 times higher than that of the other component; similar values were obtained for model A4. This indicates that the 4-keV component dominates over the entire SXS band and that one-temperature modelling is already a good approximation for the observed region in this bandpass, although the presence of a multi-temperature plasma was previously inferred for this cluster^{43,44}. We also treated the absorption columns and the AGN spectral index and flux as free parameters and confirmed no significant change in the relative abundances of the Fe-peak elements. Finally, we used the SPEX atomic code⁴⁵ v.3.03 to fit the same spectral data with the same model components and assumptions (models S1–S4, equivalent to models A1–A4, respectively). The measured abundance ratios for each model are summarized in Extended Data Fig. 3. The ranges between the minimum and maximum values determined by models A1–A4 and S1–S4 are given in Fig. 2 as the systematic uncertainty for the abundance ratio of each element (thin black error bars). The systematic uncertainties due to the different atomic databases and assumptions are larger than the statistical errors but reasonably small for most of the elements. All the metal abundances are found to be fairly consistent with the solar values²⁵. There are no significant differences in abundances derived from the analysis of a region that excludes the $2' \times 2'$ box centred on the AGN of NGC 1275 (Hitomi Collaboration, manuscript in preparation).

We have found that the abundance ratios of Cr/Fe, Mn/Fe and Ni/Fe are systematically lower than those determined in recent XMM-Newton studies¹¹. Because an old plasma model (SPEX v.2.05) was used in this previous work, we also fitted the SXS spectrum using that model for direct comparison. The results from one- and two-temperature modelling with the resonance-scattering correction are given in Extended Data Fig. 3 (models S'1 and S'3, respectively) and Extended Data Fig. 4 (red diamonds) with the combined uncertainty ranges. The Cr and Mn abundances are not presented, because the SPEX v.2.05 atomic code does not contain emission from these elements—in the previous work, these abundances were calculated by referring to emissivity data in an early version of SPEX v.3. The Ni abundance determined from this old atomic model is slightly higher than that calculated with the latest version (SPEX v.3.03), but still lower than the XMM-Newton results. In fact, there is little difference between SPEX v.2.05 and v.3.03 in the Ni He α emissivity. We find considerable differences between the two SPEX versions in the line emissivities of Fe xxiv and the Fe xxv complex at the rest-frame energies of 7.6–7.9 keV. Given that these emission lines cannot be separated from the Ni resonance line in CCD spectra, the Ni abundance might have been biased in the previous measurements.

Because Cr and Mn are rarely detected from individual objects with CCD observations, it is not obvious whether the supersolar abundances derived from the integrated XMM-Newton data of the 44 objects are correct or biased. On the other hand, observations made with similar CCDs on board the Suzaku observatory detected these elements in the same Perseus core region as in this work³⁹. The Suzaku-measured abundances (green squares), normalized using the up-to-date solar abundance table²⁵, are compared with the Hitomi and XMM-Newton results in Extended Data Fig. 4. This earlier measurement of the Mn/Fe ratio is significantly lower than our result, motivating the following demonstration of the robustness of our measurements compared to that of CCD observations.

Extended Data Fig. 5a shows the SXS spectrum near the Cr and Mn emission lines, which have equivalent widths of only a few electronvolts. The red line indicates our best-fitting model (model A1) with the Cr and Mn abundances set to zero. As shown in the bottom panel of Extended Data Fig. 5a, the photon count ratio between the peak and the local continuum level is approximately 1.2

for these weak emission lines in this high-resolution spectrum. Extended Data Fig. 5b shows a similar plot, but the spectrum is convolved to the resolution of CCDs using a representative XMM-Newton response function. Unlike the SXS spectrum, the peak-to-continuum level ratios for the Cr and Mn emissions are extremely low (only a few per cent above unity). Moreover, the emission lines no longer have a sharp profile, making it difficult to separate them from the continuum. In fact, if we fitted this simulated CCD spectrum with a model with 1% higher (or lower) continuum normalization, the line components with their broad profiles would ‘compensate’ for the excess (or lack) of continuum flux by requiring about 50% lower (or higher) values of the Cr/Fe and Mn/Fe abundance ratios. The high-resolution SXS spectrum is much less subject to such systematic uncertainties because the line and continuum intensities are measured almost independently; hence, a slight over- or under-estimation of the continuum level has little effect on the abundance measurement. This point is illustrated quantitatively in Extended Data Fig. 6, which shows the result of our test analysis.

Comparison with supernova nucleosynthesis models. The measured abundances of the Fe-peak elements are compared with theoretical predictions to determine the nature of type Ia supernovae that may have contributed to the chemical enrichment in the Perseus cluster. As prototype type Ia supernova models, we select those used in the latest three-dimensional calculations of refs 12 and 13. The former (model N100) assumes a delayed-detonation explosion of a near- M_{Ch} white dwarf with 100 deflagration ignition sites. The latter (model 1.1_0.9 in Extended Data Tables 3, 4) assumes the violent merger of two sub- M_{Ch} white dwarfs with masses of $1.1M_{\odot}$ and $0.9M_{\odot}$ and the subsequent full detonation of the primary (more massive) white dwarf. Both models successfully replicate the typical observables of type Ia supernovae, including the average maximum brightness and synthesized ^{56}Ni mass of approximately $0.6M_{\odot}$. The pre-explosion white dwarf is composed of 47.5% ^{12}C , 50% ^{16}O and 2.5% ^{22}Ne by mass, which corresponds to nearly solar metallicity for the progenitor. As another example of a sub- M_{Ch} explosion, we choose the 10HC model from ref. 14, which assumes an explosion of a single carbon–oxygen white dwarf with a mass of $1.0M_{\odot}$ accreting helium at a rate of $\dot{M}=4.0 \times 10^{-8}M_{\odot}\text{yr}^{-1}$. An initial detonation ignited in the helium layer triggers a second detonation in the C–O core, resulting in a complete explosion of the white dwarf with a kinetic energy of 1.2×10^{51} erg and ^{56}Ni mass of about $0.64M_{\odot}$, as typically inferred for type Ia supernovae.

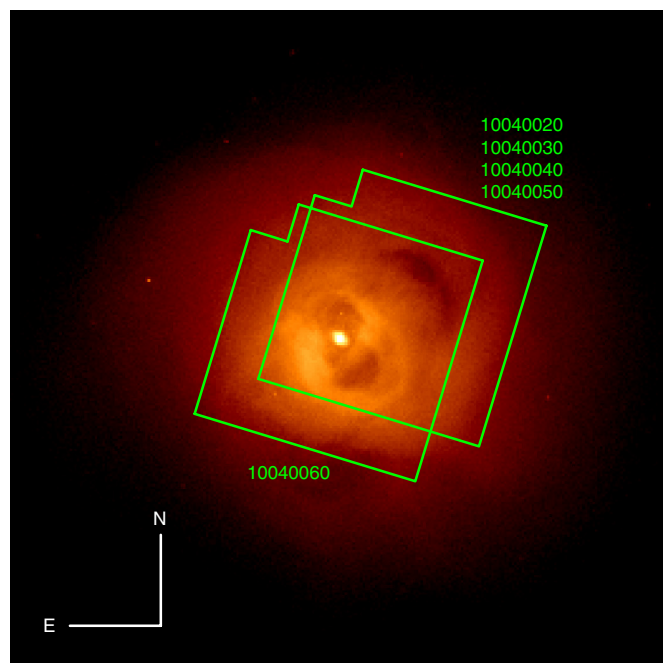
To account for the core-collapse supernova contributions, we consider mass-dependent yields²⁷ weighted by the Salpeter IMF (slope $\alpha=2.35$), with the assumption that 50% of stars with masses of at least $25M_{\odot}$ explode as hypernovae. Because type Ia supernovae produce Fe efficiently, whereas core-collapse supernovae dominate α -element production, the SXS spectra that we extracted could be used to constrain the type Ia supernova/core-collapse ratio in the Perseus cluster. However, instead of determining the actual f_{CC} value, we allow a conservatively wide range for the core-collapse supernova fraction, $f_{\text{CC}} \equiv N_{\text{CC}}/(N_{\text{Ia}} + N_{\text{CC}}) = 0.6\text{--}0.9$ (refs 2, 9, 19, 28, 29, 46, 47). This choice was made because (1) the lighter elements that are most sensitive to f_{CC} (that is, O, Ne and Mg) were not detected owing to the attenuation of soft X-rays by the closed aperture window; (2) the measured abundances of the intermediate-mass α -burning elements, unlike those of the Fe-peak elements, are dominated by systematic, rather than statistical, uncertainties (Extended Data Fig. 3); and (3) the primary origins of Ar and Ca are currently under debate^{3,48}. Future high-resolution X-ray spectroscopy with sensitivity to softer X-rays will improve the accuracy of the abundances of the lighter elements, as well as that of the ICM spectral model, hence allowing better constraints on the type Ia/core-collapse supernova ratio. We emphasize that, in contrast to the intermediate-mass α -burning elements, the abundances of the Fe-peak elements are robustly determined with little model dependency (Extended Data Fig. 3). As a result, the main conclusions of this paper are not affected by any of the issues described above.

The abundance ratios predicted by the model calculations are given in Fig. 3. Because of the efficient electron capture and the low-entropy freeze-out from nuclear statistical equilibrium⁵, higher abundances of Mn and Ni are expected in the near- M_{Ch} type Ia supernovae. We also tested other combinations of supernova models and different IMF slopes (for core-collapse supernovae). Extended Data Table 3 summarizes the mass ratios of the Fe-peak elements and Fe yields (in M_{\odot}) predicted by the various type Ia supernova models that we investigated^{14,6,12–14,49–53}. Because this paper discusses exclusively the products of electron capture, we consider only recent calculations that were based on up-to-date weak interaction

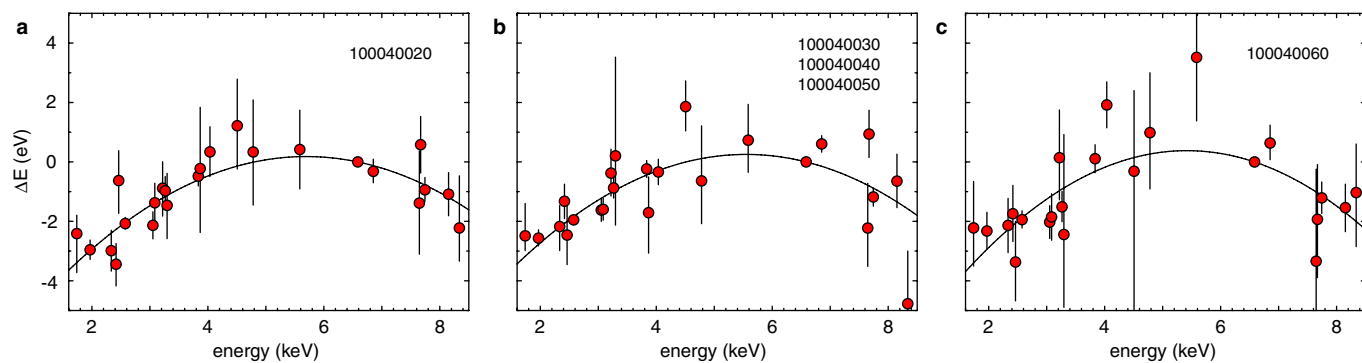
rates⁵⁴. For core-collapse supernova models, we use different IMF slopes ($\alpha=2.0$ and 2.7) and assume that all $10M_{\odot}$ – $50M_{\odot}$ stars explode as normal supernovae, without any hypernova contribution. These results are summarized in Extended Data Table 4. We reach essentially the same conclusion as that described in the main text; higher mass ratios of Mn/Fe and Ni/Fe are always expected for near- M_{Ch} type Ia supernovae (Extended Data Table 3), and a combination of near- M_{Ch} and sub- M_{Ch} type Ia supernovae explains the observed abundance pattern of the Fe-peak elements independently of contributions from core-collapse supernovae (Extended Data Table 4).

Data and code availability. The observational data analysed during this study are available in the NASA HEASARC repository (<https://heasarc.gsfc.nasa.gov/docs/hitomi/archive/>). The atomic databases used in this study are also available online (AtomDB, <http://www.atomdb.org/>, SPEX, <https://www.sron.nl/astrophysics-spez>).

- Eckart, M. E. *et al.* Ground calibration of the Astro-H (Hitomi) soft x-ray spectrometer. *Proc. SPIE* **9905**, 99053W (2016).
- Angelini, L. *et al.* Astro-H data analysis, processing and archive. *Proc. SPIE* **9905**, 990514 (2016).
- Leutenegger, M. A. *et al.* In-flight verification of the calibration and performance of the ASTRO-H (Hitomi) Soft X-Ray Spectrometer. *Proc. SPIE* **9905**, 99053U (2016).
- Kelley, R. L. *et al.* The Astro-H high resolution soft x-ray spectrometer. *Proc. SPIE* **9905**, 99050V (2016).
- Porter, F. S. *et al.* In-flight performance of the Soft X-ray Spectrometer detector system on Astro-H. *Proc. SPIE* **9905**, 99050W (2016).
- Ferruit, P., Adam, G., Binette, L. & Pécontal, E. TIGER observations of the low and high velocity components of NGC 1275. *New Astron.* **2**, 345–363 (1997).
- Okajima, T. *et al.* First peek of ASTRO-H Soft X-ray Telescope (SXT) in-orbit performance. *Proc. SPIE* **9905**, 99050Z (2016).
- Cash, W. Parameter estimation in astronomy through application of the likelihood ratio. *Astrophys. J.* **228**, 939–947 (1979).
- Tamura, T. *et al.* X-ray spectroscopy of the core of the Perseus cluster with Suzaku: elemental abundances in the intracluster medium. *Astrophys. J.* **705**, L62–L66 (2009).
- Foster, A. R., Ji, L., Smith, R. K. & Brickhouse, N. S. Updated atomic data and calculations for X-ray spectroscopy. *Astrophys. J.* **756**, 128 (2012).
- Churazov, E., Forman, W., Jones, C., Sunyaev, R. & Böhringer, H. XMM-Newton observations of the Perseus cluster - II. Evidence for gas motions in the core. *Mon. Not. R. Astron. Soc.* **347**, 29–35 (2004).
- Kalberla, P. M. W. *et al.* The Leiden/Argentine/Bonn (LAB) Survey of Galactic HI. Final data release of the combined LDS and IAR surveys with improved stray-radiation corrections. *Astron. Astrophys.* **440**, 775–782 (2005).
- Zhuravleva, I. *et al.* Resonant scattering in the Perseus Cluster: spectral model for constraining gas motions with Astro-H. *Mon. Not. R. Astron. Soc.* **435**, 3111–3121 (2013).
- Sanders, J. S. & Fabian, A. C. A deeper X-ray study of the core of the Perseus galaxy cluster: the power of sound waves and the distribution of metals and cosmic rays. *Mon. Not. R. Astron. Soc.* **381**, 1381–1399 (2007).
- Kaastra, J. S., Mewe, R. & Nieuwenhuijzen, H. In *UV and X-ray Spectroscopy of Astrophysical and Laboratory Plasmas* (eds Yamashita, K. & Watanabe, T.) 411–414 (Universal Academy Press, 1996).
- Simionescu, A. *et al.* Chemical enrichment in the cluster of galaxies Hydra A. *Astron. Astrophys.* **493**, 409–424 (2009).
- Ezer, C. *et al.* Uniform contribution of supernova explosions to the chemical enrichment of Abell 3112 out to R_{200} . *Astrophys. J.* **836**, 110 (2017).
- Mulchaey, J. S., Kasliwal, M. M. & Kollmeier, J. A. Calcium-rich gap transients: solving the calcium conundrum in the intracluster medium. *Astrophys. J.* **780**, L34 (2013).
- Fink, M. *et al.* Three-dimensional pure deflagration models with nucleosynthesis and synthetic observables for Type Ia supernovae. *Mon. Not. R. Astron. Soc.* **438**, 1762–1783 (2014).
- Travaglio, C., Hillebrandt, W., Reinecke, M. & Thielemann, F.-K. Nucleosynthesis in multi-dimensional SN Ia explosions. *Astron. Astrophys.* **425**, 1029–1040 (2004).
- Travaglio, C., Röpke, F. K., Gallino, R. & Hillebrandt, W. Type Ia supernovae as sites of the p-process: two-dimensional models coupled to nucleosynthesis. *Astrophys. J.* **739**, 93 (2011).
- Bravo, E. & Martínez-Pinedo, G. Sensitivity study of explosive nucleosynthesis in type Ia supernovae: Modification of individual thermonuclear reaction rates. *Phys. Rev. C* **85**, 055805 (2012).
- Tsujimoto, T. & Shigeyama, T. Diversity of Type Ia supernovae imprinted in chemical abundances. *Astrophys. J.* **760**, L38 (2012).
- Langanke, K. & Martínez-Pinedo, G. Shell-model calculations of stellar weak interaction rates: II. Weak rates for nuclei in the mass range $A=45\text{--}65$ in supernovae environments. *Nucl. Phys. A* **673**, 481–508 (2000).

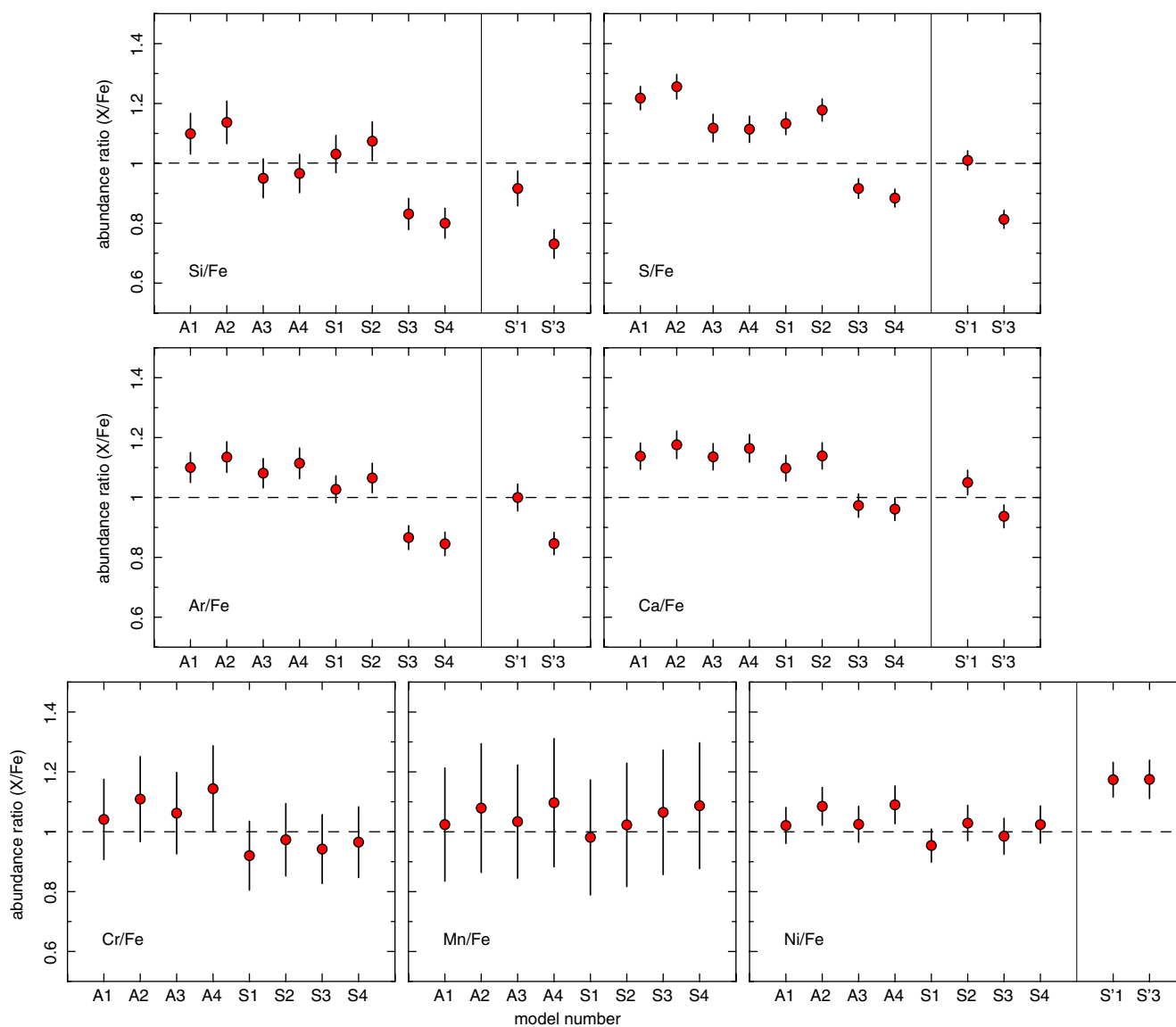


Extended Data Figure 1 | The SXS field of view overlaid on a Chandra image in the 1.8–9.0 keV band. The corresponding sequence IDs of the Hitomi observations are given. Each side of the SXS field of view has an angular size of 3' (about 64 kpc).



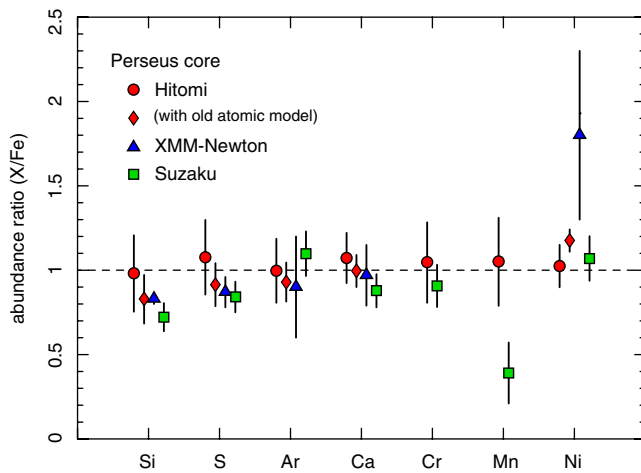
Extended Data Figure 2 | Additional gain correction. **a–c,** The data points indicate the difference $\Delta E = E' - E_0$ between the measured (E') and theoretical (E_0) energies of each detected line at the given X-ray energy. The best-fitting parabolic functions are given as solid curves. The error

bars correspond to the 1σ confidence level. **a, b** and **c** show the results from sequence 100040020, 100040030–50 (combined) and 100040060, respectively.

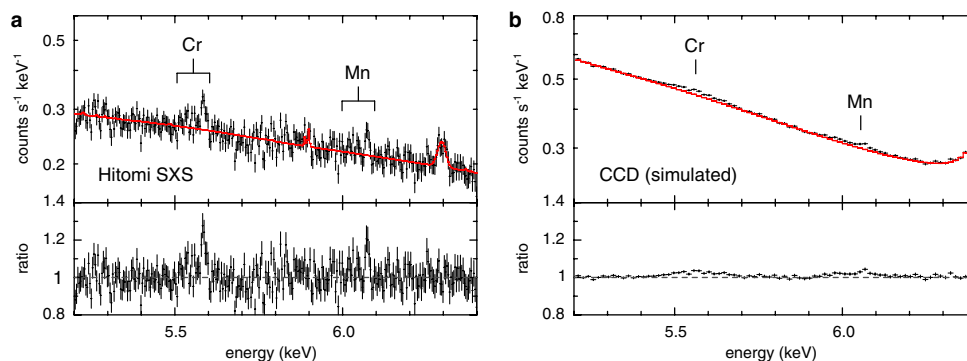


Extended Data Figure 3 | Elemental abundances calculated with different model assumptions. 'A' and 'S' indicate the results obtained using the atomic databases AtomDB v.3.0.8 and SPEX v.3.0.3, respectively, and 'S' represents an old atomic model (SPEX v.2.05, which does not contain Cr and Mn line data). Numerical designations are as follows:

'1', one-temperature fit with the Fe xxv resonance-scattering effect;
 '2', one-temperature fit without the resonance-scattering effect;
 '3', two-temperature fit with the resonance-scattering effect;
 '4', two-temperature fit without the resonance-scattering effect.
 The error bars correspond to the 1σ confidence level.

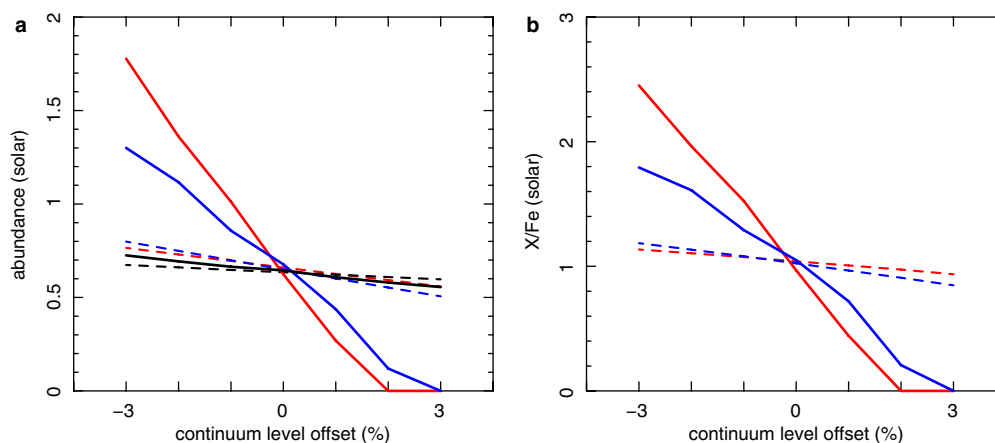


Extended Data Figure 4 | Elemental abundances of the Perseus cluster core from different X-ray measurements. Relative abundances with respect to Fe (X/Fe , $X = Si, S, Ar, Ca, Cr, Mn, Ni$) normalized to the corresponding solar abundances²⁵ (dashed line). The red circles are identical to those in Fig. 2 and represent the SXS measurements, with error bars that include both the 1σ statistical uncertainty and systematic uncertainty. The red diamonds show the same SXS measurements analysed with an outdated atomic model that was used in the XMM-Newton study. The blue triangles represent the XMM-Newton results¹¹, as in Fig. 2. The green squares are abundances obtained from Suzaku observations of the innermost $2'$ region of the Perseus cluster³⁹, converted using the updated solar abundance table²⁵ for direct comparison with the other measurements. The error bars are also converted to represent the statistical uncertainty at a 1σ confidence level.



Extended Data Figure 5 | Weak emission lines at different energy resolutions. **a**, SXS spectrum of the Perseus cluster around the Cr and Mn emission. The red line is the best-fitting model (model A1) with the Cr and Mn abundances set to zero. The bottom panel shows the ratio between the data and the model results. The error bars correspond to the 1σ confidence

level. **b**, Simulated spectrum at the typical energy resolution of the XMM-Newton CCD data (MOS1 detector), assuming the best-fitting model for the SXS data and sufficiently long exposure time (4 Ms). This comparison demonstrates the robustness of our measurements of weak emission lines with high-resolution spectroscopy (see Methods for details).



Extended Data Figure 6 | Effect of potential bias in the continuum-level estimate on the abundance measurement using weak emission lines. **a**, Abundances of Cr (red), Mn (blue) and Fe (black) determined by intentionally adding a small offset to the continuum normalization (within $\pm 3\%$ of the measured value). The solid and dashed lines are obtained from our test analysis of the simulated CCD spectrum (Extended Data Fig. 5b) and the Hitomi spectrum, respectively.

This illustrates that the CCD measurement of Cr and Mn abundances is sensitive to the accuracy of the continuum-level determination because of the weakness of the emission and the low spectral resolution. The Fe abundance is less subject to such uncertainty, even in the CCD measurement, owing to the much larger equivalent width of the emission. **b**, Abundance ratios of Cr/Fe (red) and Mn/Fe (blue), calculated using the values in **a** as a function of offset in the continuum level.

Extended Data Table 1 | Summary of the observations

Sequence ID	Observation Start Time	Pointing R.A. (deg)	Pointing Dec. (deg)	Exposure Time (ks)
100040020	2016-02-25 02:14:12	49.9316	41.5194	97.44
100040030	2016-03-04 02:17:32	49.9324	41.5201	72.51
100040040	2016-03-05 12:00:15	49.9321	41.5199	68.13
100040050	2016-03-06 19:37:59	49.9323	41.5215	5.45
100040060	2016-03-06 22:56:19	49.9510	41.5123	45.79
Total				289.32

Sequences 100040030, 100040040 and 100040050 are continuous observations, separated for data processing reasons. R.A., right ascension; dec., declination.

Extended Data Table 2 | Solar abundance table used in this work

Element	Relative Number
H	1.00
He	9.71×10^{-2}
Si	3.85×10^{-5}
S	1.62×10^{-5}
Ar	3.57×10^{-6}
Ca	2.33×10^{-6}
Cr	5.05×10^{-6}
Mn	3.56×10^{-6}
Fe	3.27×10^{-5}
Ni	1.89×10^{-6}

Data are from ref. 25.

Extended Data Table 3 | Mass ratios of the Fe-peak elements in type Ia supernova models

Model	Cr/Fe	Mn/Fe	Ni/Fe	Fe mass (M_{\odot})	Reference
Near- M_{Ch} SN Ia models					
N40	0.012	0.016	0.095	0.78	12
N100	0.014	0.018	0.10	0.74	12
N150	0.015	0.020	0.11	0.71	12
N40def	0.0092	0.022	0.14	0.44	49
N100def	0.0094	0.022	0.14	0.47	49
N150def	0.0094	0.022	0.14	0.50	49
W7	0.0069	0.0088	0.16	0.76	4
CDEF	0.0092	0.019	0.22	0.39	4
CDDT	0.0098	0.017	0.21	0.36	4
ODDT	0.016	0.011	0.12	0.65	4
c3_2d_512	0.0078	0.018	0.22	0.32	50
c3_2d_256	0.0084	0.015	0.21	0.41	50
c3_3d_256	0.0082	0.013	0.20	0.41	50
b5_3d_256	0.011	0.011	0.16	0.40	50
b30_3d_768	0.0060	0.012	0.20	0.53	50
DDTa	0.019	0.020	0.099	0.72	51
Sub- M_{Ch} SN Ia models					
1.1_0.9	0.011	0.0059	0.050	0.65	13
10HC	0.012	0.0023	0.032	0.63	14
10HCD	0.028	0.0034	0.037	0.61	14
10HD	0.018	0.0025	0.041	0.65	14
11HD	0.0076	0.0014	0.038	0.76	14
10B	0.017	0.0022	0.039	0.73	14
10C	0.014	0.0021	0.044	0.69	14
10D	0.0098	0.0017	0.046	0.74	14
9B	0.026	0.0034	0.050	0.61	14
9C	0.021	0.0028	0.040	0.64	14
9D	0.018	0.0024	0.044	0.66	14
1.06 M_{\odot}	0.031	0.0059	0.059	0.76	6 (52)
0.97 M_{\odot}	0.013	0.0092	0.051	0.58	6 (52)
0.8 M_{\odot} + 0.6 M_{\odot}	0.017	0.0027	0.019	0.41	53

Extended Data Table 4 | Example calculations of supernova nucleosynthesis models

Near- M_{Ch}	Sub- M_{Ch}	CC	IMF	f_{CC}	$f_{M_{\text{Ch}}}$	$f_{\text{Fe, Ia}}$	Cr/Fe	Mn/Fe	Ni/Fe
Near- M_{Ch} SNe Ia only									
N100	—	SN+HN	2.35	0.60	1.0	0.85	0.98	1.51	1.54
N100	—	SN+HN	2.35	0.90	1.0	0.49	1.00	1.08	1.23
N100	—	SN+HN	2.0	0.60	1.0	0.84	0.99	1.50	1.54
N100	—	SN+HN	2.0	0.90	1.0	0.47	1.04	1.07	1.23
N100	—	SN+HN	2.7	0.60	1.0	0.86	0.97	1.52	1.55
N100	—	SN+HN	2.7	0.90	1.0	0.50	0.98	1.10	1.24
N100	—	SN only	2.35	0.60	1.0	0.87	1.01	1.54	1.54
N100	—	SN only	2.35	0.90	1.0	0.52	1.14	1.17	1.21
Sub- M_{Ch} SNe Ia only									
—	1.1_0.9	SN+HN	2.35	0.60	0.0	0.83	0.81	0.55	0.83
—	1.1_0.9	SN+HN	2.35	0.90	0.0	0.45	0.92	0.53	0.83
—	1.1_0.9	SN+HN	2.0	0.60	0.0	0.82	0.82	0.55	0.84
—	1.1_0.9	SN+HN	2.0	0.90	0.0	0.44	0.95	0.54	0.84
—	1.1_0.9	SN+HN	2.7	0.60	0.0	0.84	0.80	0.54	0.83
—	1.1_0.9	SN+HN	2.7	0.90	0.0	0.47	0.89	0.53	0.82
—	1.1_0.9	SN only	2.35	0.60	0.0	0.85	0.85	0.56	0.82
—	1.1_0.9	SN only	2.35	0.90	0.0	0.48	1.05	0.59	0.77
—	10HC	SN+HN	2.35	0.60	0.0	0.83	0.86	0.27	0.59
—	10HC	SN+HN	2.35	0.90	0.0	0.45	0.95	0.38	0.69
—	10HC	SN+HN	2.0	0.60	0.0	0.82	0.88	0.27	0.59
—	10HC	SN+HN	2.0	0.90	0.0	0.43	0.98	0.39	0.71
—	10HC	SN+HN	2.7	0.60	0.0	0.84	0.85	0.26	0.58
—	10HC	SN+HN	2.7	0.90	0.0	0.46	0.92	0.37	0.68
—	10HC	SN only	2.35	0.60	0.0	0.85	0.90	0.28	0.57
—	10HC	SN only	2.35	0.90	0.0	0.48	1.09	0.43	0.63
Both contributions of near- and sub- M_{Ch} SNe Ia									
N100	1.1_0.9	SN+HN	2.35	0.60	0.5	0.84	0.90	1.05	1.21
N100	1.1_0.9	SN+HN	2.35	0.90	0.5	0.47	0.96	0.81	1.04
N100	1.1_0.9	SN only	2.35	0.60	0.5	0.86	0.94	1.08	1.20
N100	1.1_0.9	SN only	2.35	0.90	0.5	0.50	1.10	0.89	1.00
N100	10HC	SN+HN	2.35	0.60	0.5	0.84	0.92	0.93	1.10
N100	10HC	SN+HN	2.35	0.90	0.5	0.47	0.98	0.74	0.97
N100	10HC	SN only	2.35	0.60	0.5	0.86	0.96	0.95	1.09
N100	10HC	SN only	2.35	0.90	0.5	0.50	1.11	0.81	0.93

The first three columns indicate the name and combination of supernova models and the fourth column presents the assumed index of the IMF. $f_{\text{CC}} = N_{\text{CC}} / (N_{\text{Ia}} + N_{\text{CC}})$, $f_{M_{\text{Ch}}} = N_{M_{\text{Ch}}} / N_{\text{Ia}}$ and $f_{\text{Fe, Ia}}$ are the number fraction of core-collapse supernovae, the number fraction of near- M_{Ch} type Ia supernovae and the mass fraction of Fe originating from type Ia supernovae, respectively. The remaining columns indicate abundance ratios relative to the solar values²⁵. SN, supernova; HN, hypernova.